Astron. Astrophys. 352, 670–678 (1999)

ASTRONOMY AND ASTROPHYSICS

Fast solar wind acceleration by Alfvén waves: observable effects on the EUV lines detected by SOHO/UVCS

R. Ventura[1], **S. Orlando**[2,3], **G. Peres**[2], **and D. Spadaro**[1]

[1] Osservatorio Astrofisico, Città Universitaria, V. le A. Doria 6, 95125 Catania, Italy
[2] Dipartimento di Scienze Fisiche ed Astronomiche, Sezione di Astronomia, Piazza del Parlamento 1, 90134 Palermo, Italy
[3] Solar System Division, ESA Space Science Department, ESTEC, Postbus 299, 2200 AG Noordwijk, The Netherlands

Received 12 February 1999 / Accepted 27 October 1999

Abstract. SOHO/UVCS observations of the most intense EUV spectral lines emitted by the solar corona have been providing us a good opportunity to study in detail the acceleration regions of the solar wind. In this work we aim at deriving useful diagnostics and identifying possible signatures of Alfvén waves momentum deposition. More specifically we investigate, with the help of a detailed wind model (Orlando et al. 1996), the insight and the constraints that these observations give on the presence of Alfvén waves, as deduced from the influence of the waves on the solar wind structure and dynamics.

The model developed by Orlando et al. (1996) accounts for the momentum deposition by a spectrum of non-WKB Alfvén waves, generated in the Sun's lower atmosphere and undergoing significant reflection across the transition region. We compute a set of wind solutions characterized by different physical conditions, synthesize, from them, the emission in the Lyα, Lyβ and O VI doublet (1032 Å, 1038 Å) lines and derive possible diagnostics. We finally compare our results with the most recent SOHO/UVCS data.

Key words: Sun: corona – Sun: solar wind – Sun: UV radiation

1. Introduction

The problem of the acceleration of the fast solar wind streams, originating from coronal holes, is one of the puzzles of solar physics. In spite of a great deal of theoretical work devoted to this topic, the process (or processes) responsible for the release of the additional momentum and energy required to drive the wind up to the observed high flow speeds (700–800 km s^{-1} at 1 AU) is still far from being ascertained. In this context, among other mechanisms proposed (e.g. Axford & McKenzie 1992; McKenzie et al. 1995; Esser et al. 1997), the interaction between Alfvén waves of solar origin and the ambient coronal plasma has attracted considerable interest in recent years (e.g. Hollweg 1990; Musielak et al. 1992; Velli 1993; Mac Gregor & Charbonneau 1994). It was found that Alfvén waves, generated presumably through magnetic footpoint shuffling at the photospheric level and propagating into the interplanetary space (see Withbroe 1988), can experience significant reflection across the transition region (An et al. 1989; Moore et al. 1991). This effect may cause a momentum and energy deposition taking place within a few solar radii from the Sun which, in principle, can accelerate the solar wind to the observed high speed values (Orlando et al. 1996). As a consequence Alfvén waves, if really present in the corona, may influence the coronal structure and dynamics and, ultimately, the intensities and profiles of emission lines formed there (Maltby 1968; Withbroe et al. 1982; Sandbæk & Leer 1994; Olsen et al. 1994).

The recent availability of outer solar corona observations by the Ultraviolet Coronagraph Spectrometer (UVCS, Kohl et al. 1995), on board the SOlar and Heliospheric Observatory (SOHO, Domingo et al. 1995), gives us a great opportunity of constraining the models of heating and acceleration of the solar wind: UVCS observations of strong EUV emission lines provide diagnostics of plasma physical parameters (e.g. density, temperature and outflow speed) in the coronal structures where the solar wind originates (Kohl & Withbroe 1982; Withbroe et al. 1982; Noci et al. 1987).

In the light of the completely new capabilities offered by the SOHO/UVCS, we here investigate the effects of Alfvén waves momentum deposition on the physical properties of a wind model and then explore the capability to infer the plasma physical parameters (temperature, density and outflow velocity radial behaviours) from spectroscopic analysis. To this end we synthesize the emission of Lyα, Lyβ and O VI (1032 Å, 1038 Å) lines, from the detailed wind model developed by Orlando et al. (1996). The aim is to identify signatures of Alfvén waves momentum deposition from the spectral features (intensities, intensity ratios and their radial dependence) of the pre-eminent EUV spectral lines observed by SOHO/UVCS and to use them as a guideline in the data analysis.

The paper is organized as follows: the description of the solar wind model is presented in Sect. 2. Sect. 3 describes the solar corona geometry adopted and the details of the spectral synthesis. The results are presented and discussed in Sect. 4, also in the light of very recent SOHO/UVCS observations, and in Sect. 5 we draw our conclusions.

Send offprint requests to: R. Ventura (rventura@alpha4.ct.astro.it)

Table 1. Wind model parameters

Solution Nr.	$n_{\rm p\odot}/10^{10}$ ($\rm cm^{-3}$)	$B_\odot$ (Gauss)	$u_\odot/10^3$ ($\rm cm\ s^{-1}$)	$H_\odot/10^{-6}$ ($\rm erg\,cm^{-3}\,s^{-1}$)	$T_{max}/10^6$ (K)	$\dot{M}/10^{-14}$ ($M_\odot\ \rm yr^{-1}$)
SET A						
1	0.5	0.1	0.28	1.02	1.3	0.28
2	0.5	1	0.30	1.02	1.3	0.30
3	0.5	3	0.49	1.09	1.3	0.50
4	0.5	10	3.34	2.04	1.4	3.4
SET B						
5	1	0.1	2.41	4.01	1.8	4.9
6	1	1	7.01	7.59	2.0	14.2
7	1	3	2.82	4.34	1.8	5.8
8	1	10	7.39	8.13	2.0	14.9
SET C						
9	5	0.1	35.3	315	5.2	358
10	5	1	35.6	318	5.2	362
11	5	3	40.7	372	5.4	412
12	5	10	67.2	716	6.7	682
13	0.8	7	3.18	3.54	1.7	5.1

2. The solar wind model

We adopt the solar wind model developed by Orlando et al. (1996). The plasma outflow is modeled starting from the base of the transition region, where T is assumed to be 2×10^4 K and the temperature gradient is set to zero; the model takes into proper account gravity stratification, thermal conduction, radiative losses and volumetric heating (via a phenomenological term). It also accounts for the momentum deposition by a spectrum of 3-D Alfvén waves in the non–WKB regime[1] (i.e. taking into account the reflection of the waves).

In the model the transonic wind solution, here considered, is uniquely determined by two free parameters, namely the plasma density and the magnetic field strength at the base of the transition region, $n_{\rm p\odot}$ and $B_\odot$, respectively. For further details on the model, refer to Orlando et al. (1996).

In this work we have explored the parameter space computing solutions for different values of $\rm n_{p\odot}$ and $\rm B_\odot$, and taking for all of them the same spectrum of Alfvén waves as the one adopted by Orlando et al. (1996). We have focused our analysis on those solutions which can better reproduce the physical conditions of the high-speed solar wind. The typical values of density ($n_{\rm p} \sim$ 2–4 $\rm cm^{-3}$) and terminal outflow velocity ($u \sim$ 700–800 $\rm km\,s^{-1}$) observed at 1 AU, of temperature in the corona ($T_{max} \sim$ 1–3 MK) and mass loss rate ($\dot{M} \sim 1$–$3 \times 10^{-14}\ M_\odot\ \rm yr^{-1}$) (Withbroe 1988; Phillips et al. 1995; Geiss et al. 1995) can be obtained, in this context, by a model with $n_{\rm p\odot} \sim 10^{10}\ \rm cm^{-3}$ and $B_\odot \sim 3$ G. Therefore we have explored the $5 \times 10^9\ \rm cm^{-3} \leq n_{p\odot} \leq 5 \times 10^{10}\ cm^{-3}$, and 0.1 G $\leq B_\odot \leq$ 10 G ranges, around such reference values.

In Table 1 we list the set of solutions considered in our analysis; each of them is identified by density, magnetic field strength, velocity, volumetric heating at the base of the transition region; the derived values of temperature and mass loss rate in the corona are also reported. Note that the solutions which approximately satisfy the constraints on $\rm T_{max}$ and $\dot{M}$ simultaneously are the solutions 4 of set A, 5 and 7 of set B, and 13, while the others do not satisfactorily reproduce the observations. The most significant differences (of about two orders of magnitude in $\dot{M}$) occur for the solutions of set C; none the less we have taken them into account to show the role of the parameters in determining the solutions space here considered.

Solution 13 ($n_{\rm p\odot}$ = $8 \times 10^9\ \rm cm^{-3}$ and $\rm B_\odot$ = 7 G) was also considered for reasons which will be evident in the course of the discussion.

Fig. 1 shows the radial profiles of density (Fig. 1a), temperature (Fig. 1b) and outflow speed (Fig. 1c) of the solar wind solutions.

Fig. 2 shows the ratio between the contribution to the acceleration due to the Alfvén waves and that due to thermal driving, vs. the heliocentric distance, for all the model solutions. The Alfvén waves momentum deposition seems to accelerate the wind more effectively for solutions with high values of $\rm B_\odot$ (7–10 G) and values of $\rm n_{p\odot}$ not larger than $10^{10}\ \rm cm^{-3}$ (solution 4 showing the largest efficiency). On the contrary, for high values of $\rm n_{p\odot}$ ($5 \times 10^{10}\ \rm cm^{-3}$) and low values of $\rm B_\odot$ (0.1 G) (solution 9) the thermal driving seems to be the only efficient acceleration mechanism.

3. Spectral synthesis

Extensive sets of spectral simulations of the pre-eminent coronal EUV emission lines have already been carried out for different coronal structures (Spadaro & Ventura 1993, 1994a,b, 1996; Ventura & Spadaro 1999).

Along this line, we have computed Lyα, Lyβ and O VI doublet (1032 Å, 1038 Å) line intensities considering the two main

[1] The Wentzel–Kramers–Brillouin (WKB) approximation is applicable when the average properties of the unperturbed plasma vary on a spatial scale large compared with the wavelengths of interest.

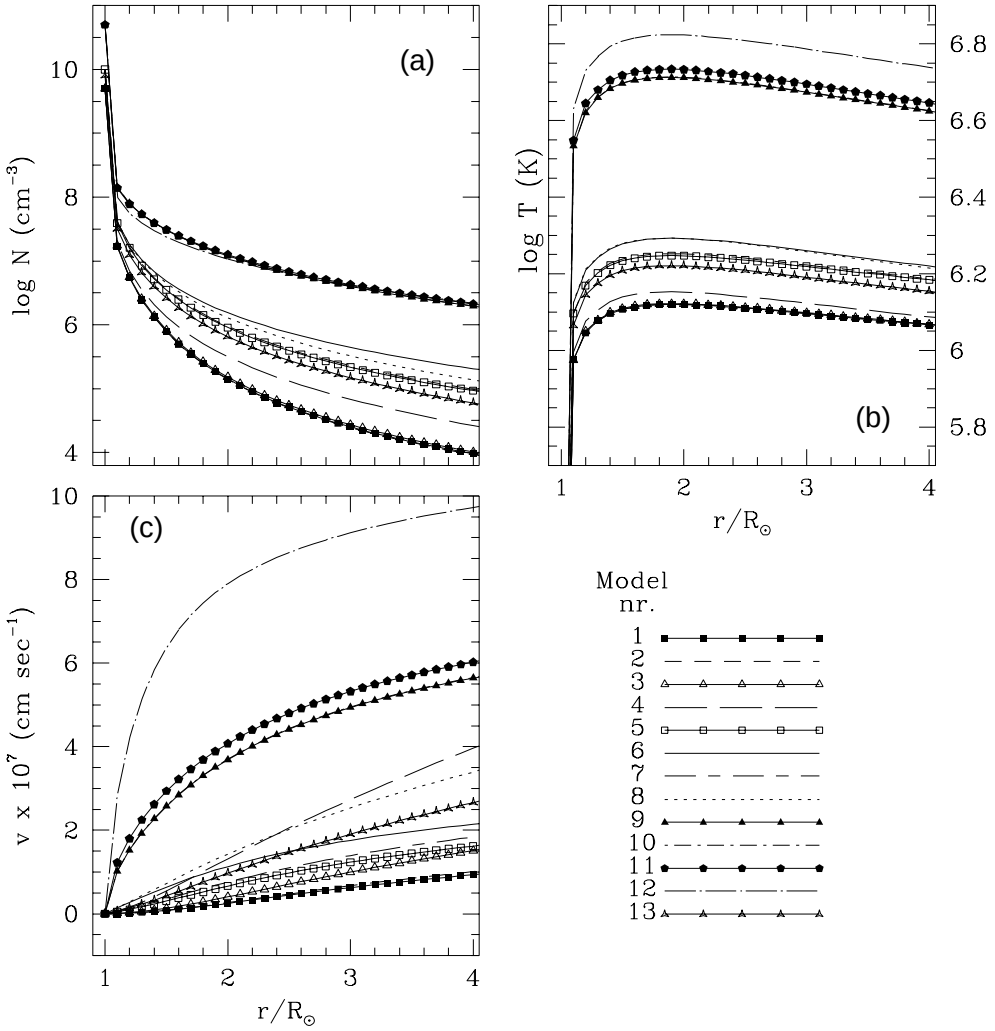

Fig. 1a–c. Radial profiles of density **a**, temperature **b** and outflow speed **c** computed for the solar wind solutions. In **a** the radial profiles of density of solutions 1 and 3 of set A are so similar to be nearly undistinguishable as it occurs for solutions 9, 10, 11 and 12 of set C. The same occurs in **b** for solutions 1, 2 and 3 of set A as well as for solutions 9 and 10 of set C and in **c** for solutions 1 and 2 of set A, and for solutions 9 and 10 of set C, respectively. Symbols adopted for the model solution identification are reported on the right bottom of the figure.

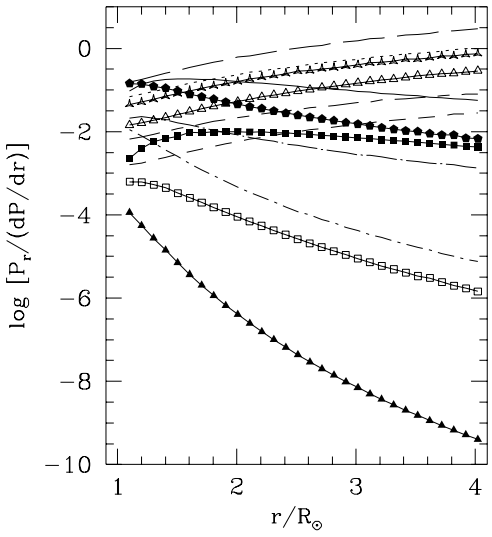

Fig. 2. Ratio of the Alfvén waves acceleration contribution P_r/ρ to the thermal driving contribution $(1/\rho)(dp/dr)$ vs. the heliocentric distance (ρ is the density and p the gas pressure). Symbols adopted to identify the model solutions are the same as reported in Fig. 1.

mechanisms of line formation (see for details Kohl & Withbroe 1982; Withbroe et al. 1982; Noci et al. 1987), i.e. the resonant scattering of chromospheric and inner corona photons by coronal ions, and the collisional excitation by electron impact.

The effect of the outflow velocity on the resonantly scattered component of each line, known as *Doppler dimming* (Beckers & Chipman 1974), has also been taken into account.

In the case of the O VI 1038 Å line, we also considered the additional excitation of the resonant component due to chromospheric photons of the two nearby C II 1037.018 Å and 1036.34 Å spectral lines (see e.g., Noci et al. 1987; Dodero et al. 1998). Their effect is important for outflow velocities of about 170 km s^{-1} and 360 km s^{-1}, respectively, i.e. high enough velocities to red-shift the C II profiles, in the coronal ion rest frame, to such an extent to overlap them with the O VI 1038 Å scattering profile.

We neglected the obvious chromospheric and coronal inhomogeneities and thus assumed the chromosphere and lower corona to be uniformly bright in the exciting radiation. We also adopted the observed intensities and profiles of the H I chromospheric Lyα and Lyβ lines reported by Gouttebroze et al. (1978). The intensities and profiles of the chromospheric O VI doublet

and C II lines are those observed by UVCS during disc measurements (Spadaro 1998). We adopted a Maxwellian velocity distribution for the emitting ions in the outflowing wind.

Our simulations were carried out modeling a coronal hole and the outgoing wind as a cone with the vertex in the centre of the Sun, the axis of symmetry located on the plane of the sky and a semi-angular extent of 35°. We also neglected any superradial expansion of the coronal hole boundaries since investigations of its effect on line intensities are beyond the scope of the present work. Within this region heliocentric radial symmetry has been assumed. Note that, according to the previuos assumption of chromosphere and low corona homogeneity, we also neglected the details of the coronal hole base spectrum in our line simulations. On the other side, we restricted our analysis to the part of the coronal hole located in the outer corona, above 1.5 $R_\odot$.

For more details and references on the formulation, the atomic data, the elemental abundances and the ionization balances, we refer to Spadaro & Ventura (1993, 1994a,b, 1996) and Ventura & Spadaro (1999).

The synthesis has been made for lines of sight intersecting the axis of symmetry of the coronal hole at heliocentric distances ranging from 1.5 to 3.5 $R_\odot$ where the UVCS observations have a good signal-to-noise ratio. The intensity values have been computed adding the contributions of all the volume elements along the line of sight within the coronal hole.

The spectral lines have been synthesized for all the 13 wind solutions described in Sect. 2, taking full account of the relevant radial distributions of density, temperature and outflow velocity.

4. Results and discussion

In order to better understand the results of our simulations, some preliminary remarks are in order. As mentioned in Sect. 3, the line intensities of EUV spectral lines are a mixture (which observations cannot directly disentangle) of the radiative and collisional components whose contributions to each spectral line strongly depend on the physical conditions of the emitting plasma.

In particular the radiative component depends linearly on the density, the collisional one on the squared density; the radiative component is affected by the Doppler dimming effect (which progressively depletes it for increasing outflow speed) with an efficiency depending, among other things, on the specific spectral line; the collisional component intensity strongly depends on the atomic parameters of the line.

In order to further clarify this point, we show in Fig. 3 the computed (*and not directly observable*) radiative-to-collisional component ratio vs. the heliocentric distance for the lines and wind solutions here considered.

The Lyα line behaviour is peculiar, in this respect, in comparison with all the other spectral lines here examined (Fig. 3a). In fact, for outflow speeds lower than 200 km s^{-1}, the collisional component is smaller, by more than two orders of magnitude, than the radiative one, giving a negligible contribution to the total intensity, for outflow speeds lower than 200 km s^{-1} (Withbroe et al. 1982; Ventura & Spadaro 1999). At higher outflow speeds the radiative component is more and more depleted by the Doppler dimming effect, so that the relative contribution of the collisional component progressively increases; it never reaches, however, high enough values to dominate the total Lyα line intensity, except for the very extreme (and probably unrealistic) physical conditions of solution 12 beyond 2–2.5 $R_\odot$.

The general behaviour and the trend vs. heliocentric distance of the ratio of the two Lyβ components are, for each solution, very similar to those of the Lyα line, except that the vertical scale is shifted downward by about two orders of magnitude (Fig. 3b). It implies that, under the same physical conditions, the contribution of the collisional component to the total intensity is more important for the Lyβ line than for the Lyα one.

The behaviour and the slope vs. heliocentric distance of the O VI radiative-to-collisional component ratio are very different in comparison with those of the two H I lines discussed before (Figs. 3c and 3d). This is due to the higher efficiency of the Doppler dimming effect in depleting the O VI lines with respect to the H I lines (see, e.g., Noci et al. 1987). Note that the radiative component of the O VI 1032 Å line is almost completely depleted and the collisional component dominates at velocities of and higher than about 200 km s^{-1} (cf. Fig. 1c).

As far as the O VI 1038 Å line is concerned (Fig. 3d), the pumping effect of the two C II chromospheric lines opposes the Doppler dimming at velocities higher than 100 km s^{-1} (Noci et al. 1987), causing the radiative-to-collisional component ratio to depend more weakly on the outflow velocity.

In the following we present and discuss the results obtained from our simulations.

4.1. Line intensities

Fig. 4 shows the total Lyα (Fig. 4a), Lyβ (Fig. 4b) and O VI doublet line intensities (Figs. 4c, d), each normalized to its maximum value, vs. the heliocentric distance, for the complete set of the wind solutions. For comparison the figure shows the most recent data on polar coronal holes obtained by SOHO/UVCS (Peres et al. 1997; Cranmer et al. 1999). The experimental data reported by Peres et al. (1997) refer to observations of the north polar coronal hole from 1.5 to 3.5 $R_\odot$ performed during a week in September 1996. Cranmer et al. (1999) present Lyα and O VI doublet lines spectroscopy obtained analyzing several scans over the north and south poles, performed during standard synoptic observations of the entire corona, between November 1996 and April 1997.

The maximum intensities, computed for each line and for each solution and corresponding to 1.5 $R_\odot$, are given in Table 2, together with the relevant observed values. The computed Lyα and O VI line intensities, at 1.5 $R_\odot$, roughly agree with the observations reported by Cranmer et al. (1999), solution 13 giving the best match with those experimental data. Solution 12, on the other hand, is the only one which seems to reproduce the observed Lyβ intensity.

In the following we first discuss the results of our simulations, separately for each line, and then compare them with the observations.

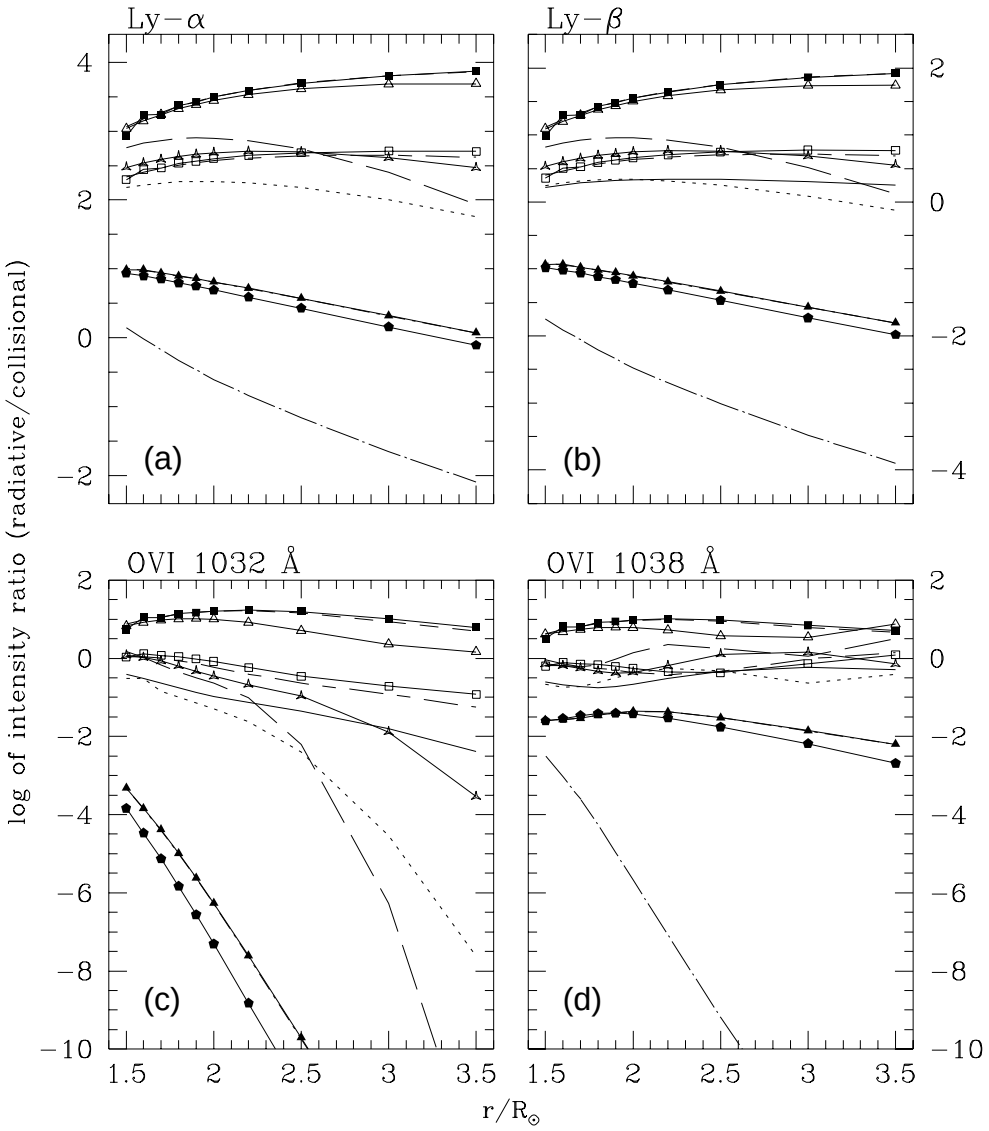

Fig. 3a–d. Radiative-to-collisional ratio vs. the heliocentric distance for Lyα **a**, Lyβ **b**, O VI 1032 Å **c** and O VI 1038 Å **d** lines for the model solutions here considered. The symbols which identify each solution are the same as in Fig. 1.

Fig. 4a, referring to the Lyα line intensities, shows that most solutions, even very different ones, exhibit a virtually identical behaviour up to 2.5 $R_\odot$, with the exception of solutions 4 (low density and steep velocity gradient), 12 (very high density and velocity values), and, to a smaller extent, 5, 6 and 7. At heliocentric distances larger than 2.5 $R_\odot$ the slope of the Lyα intensity distributions of the various solutions however differ more significantly, reflecting the differences in density (the higher the density, the less steep the slope) and outflow velocity (the higher the velocity, the steeper the slope). As a consequence the spread among the solutions increases with the heliocentric distance. Since the Lyα line is very intense and can be observed up to large heliocentric distances (at least 5–6 $R_\odot$) (Kohl et al. 1997), the differences noted above should give us the opportunity to discriminate among different physical conditions in the emitting plasma.

As far as the observational data points are concerned, the observed drop in Lyα intensity between 1.5 and 3.5 $R_\odot$ is about three orders of magnitude for both sets of observations here considered; only the results of solution 4 appear to reproduce this behaviour.

The behaviour of the Lyβ intensities (Fig. 4b) is similar to that of the Lyα one but with a larger dispersion among the different solutions, due to the higher relative contribution of the collisional component, leading to a higher line intensity dependence on the plasma density. This allows an easier discrimination among the model solutions.

The drop in the observed Lyβ intensity in the 1.5–3.0 $R_\odot$ range of heliocentric distance, as deduced by the only two experimental data points available (Peres et al. 1997), is more than two orders of magnitude, implying that only solutions 4, 8 and 13 seem to fit reasonably well the observations.

Fig. 4c shows that the spread among the various model solutions is larger for the O VI 1032 Å line than for the H I lines discussed above. In other words, the O VI distributions are influenced by the physical parameters of each solution more significantly than what occurs for H I, even for solutions of the same set. Also the global drop of the normalized intensity strongly

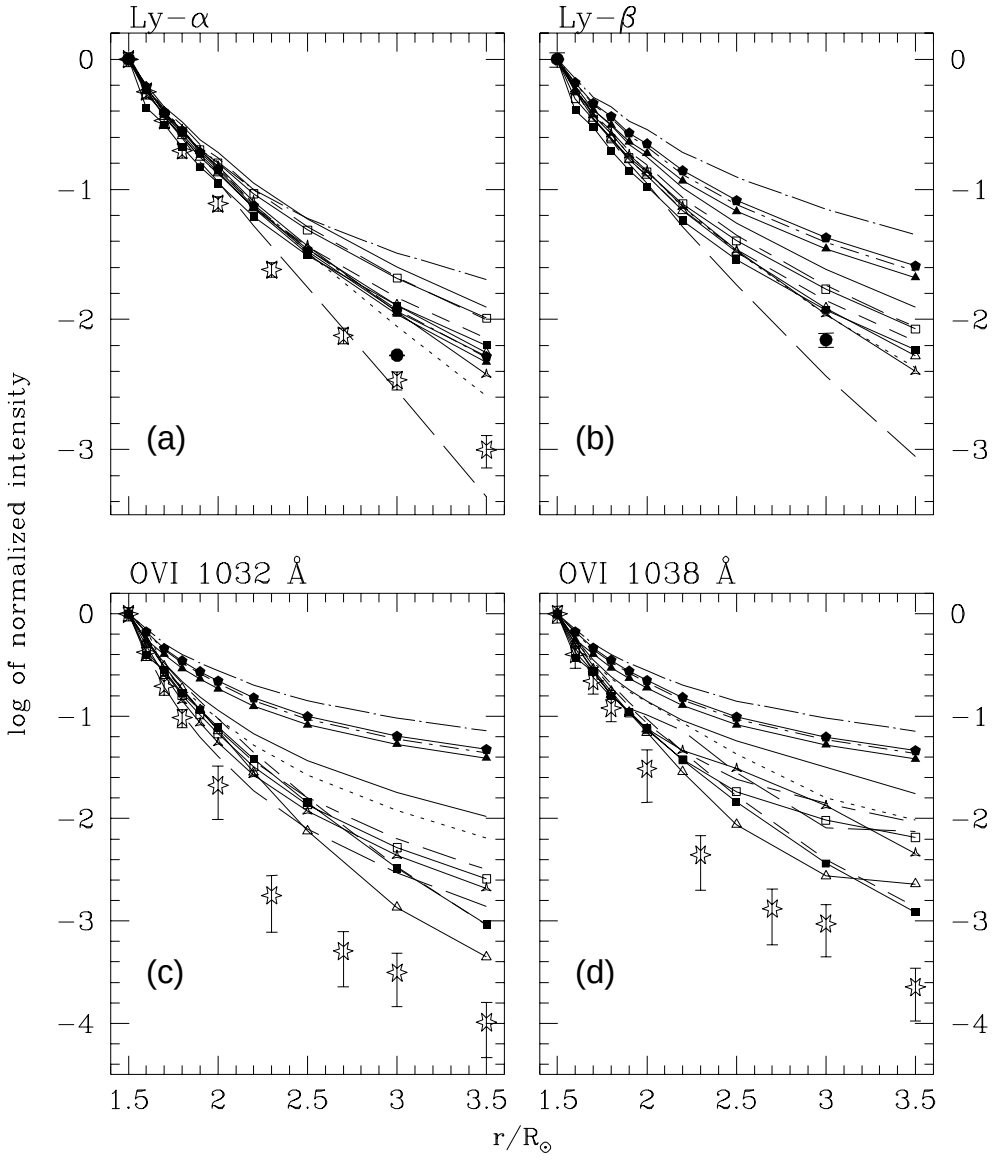

Fig. 4a–d. Line intensities of Lyα **a**, Lyβ **b**, O VI 1032 Å **c** and O VI 1038 Å **d** vs. the heliocentric distance for the complete set of examined wind solutions. For comparison with observations, the experimental data points by Peres et al. (1997) (full dots) and Cranmer et al. (1999) (stars) are also reported. In some cases the statistical error bars are too small to be discernible from the data points. All the intensities are normalized to their respective maximum value (at 1.5 $R_\odot$).

depends on the density, with the set of solutions with the lowest density (set A) giving the largest drop. The intensity distributions of model solutions in set A are determined primarily by the dependence of the Doppler dimming on the outflow velocity radial profiles, because the radiative component dominates the total line intensities (see Fig. 3c). The only exception, within this set, is solution 4 since its intensity decreases more slowly with the heliocentric distance beyond 2 $R_\odot$: the contribution of the collisional component, already significant at 1.5 $R_\odot$, considerably increases at larger heliocentric distances, until it dominates completely the O VI 1032 Å line intensity above 2.2 $R_\odot$ (see Fig. 3c). Note that, instead, the drop of H I intensity of solution 4 is by far the largest among those of set A. Since solution 4 is the most influenced one by the Alfvén waves, a comparison of the drop of intensity between 1.5 and 3.5 $R_\odot$ of H I and O VI might provide a useful diagnostics of the waves themselves.

The intensity distributions of solutions of set B and solution 13 exhibit intermediate behaviours: they are a mixture of radiative and collisional components, very close to the Sun, and are more and more collisionally dominated at larger heliocentric distances. The collisional component starts to dominate at heliocentric distances smaller and smaller as the velocities in the solutions get higher and higher (e.g., solutions 8 and 13).

The intensity distributions of solutions of set C are completely dominated by the collisional component (see Fig. 3c), hence they reflect the relevant density distributions.

The observed OVI 1032 Å line intensity of Cranmer et al. (1999) shows a drop, vs. heliocentric distance, of about four orders of magnitude; the largest drop of intensity in our simulations is little more than three orders of magnitude (solution 3 of set A).

The radial dependence of the O VI 1038 Å total line intensities is only roughly similar to that of the O VI 1032 Å line (Fig. 4d). The slight differences are due to the pumping effect by the two nearby chromospheric C II lines; the effect is evident

Table 2. Maximum intensities (1.5 $R_\odot$)

Solution nr	Intensity (erg cm^{-2} s^{-1} sr^{-1})			
	Lyα	Lyβ	O VI 1032	O VI 1038
SET A		(10^{-3})	(10^{-2})	(10^{-2})
1	0.54	1.44	3.69	1.16
2	0.45	1.16	2.92	0.90
3	0.47	1.22	2.95	0.98
4	0.68	1.88	2.29	0.88
SET B				
5	1.60	5.53	9.06	3.52
6	1.68	6.47	7.24	3.22
7	1.47	4.97	7.49	2.91
8	1.48	5.57	5.66	2.59
SET C				
9	1.97	41.8	3.18	1.62
10	1.85	37.7	2.82	1.41
11	1.56	36.3	2.37	1.20
12	0.19	16.3	0.59	0.29
13	1.16	3.59	5.12	1.98
Peres et al. (1997)	2.90 ±2.35e-03	18.6 ±0.20	–	–
Cranmer et al. (1999)	1.0 ±0.12	–	6.80 ±0.99	2.41 ±0.45

for the intensity distributions of solutions of sets A and B, and, in particular, for solutions 3, 4, 7, 8 and 13.

Similar considerations to those discussed above for the OVI 1032 Å line intensities hold when comparing simulations and observations of the OVI 1038 Å line intensity.

4.2. Line ratios

We have also computed the intensity ratio of the H I Lyα and Lyβ spectral lines, as well as of the O VI 1038 Å and 1032 Å lines. The first ratio is a strong indicator of the plasma density (Romoli & Fineschi 1994; Noci et al. 1997), the second one of the plasma outflow velocity (e.g., Noci et al. 1987).

Fig. 5 shows the Lyα/Lyβ ratio vs. heliocentric distance. The different physical conditions yield evident differences in the radial profiles. The curves of *high-density* solutions (set C) are very different from those of *low- and intermediate-density* solutions (sets A, B, and solution 13): for the solutions of set C the ratio approaches more and more the typical value for pure collisional excitation of the lines ($\simeq$ 0.68 in the logarithm scale of Fig. 5) as the heliocentric distance increases; instead for those of sets A, B and solution 13 the ratio is close to the value for pure excitation by resonant scattering in a static corona ($\simeq$ 2.62 in the logarithm scale of Fig. 5).

As for the solutions of set C, the collisional component of these lines is significant over the whole 1.5–3.5 $R_\odot$ range. The relevant curves (cf. Fig. 5) also show a clear signature of Doppler dimming: the ratio decreases steadily vs. r/$R_\odot$ because of the increasing depletion of the radiative component.

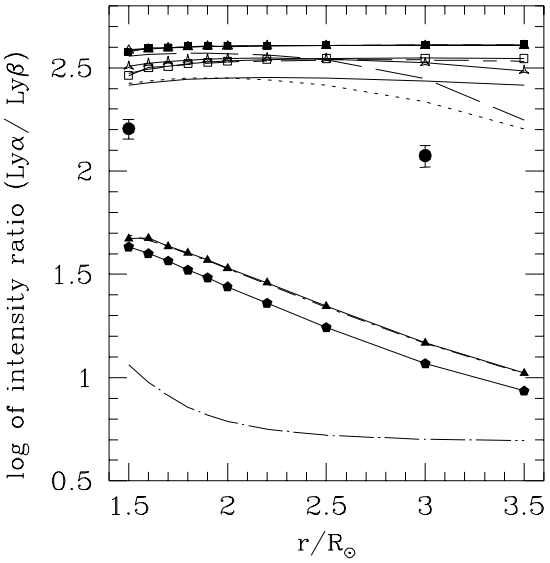

Fig. 5. Intensity ratio of the H I Lyα and Lyβ lines vs. the heliocentric distance for all the model solutions examined. Peres et al. (1997) data points (full dots) are also reported for comparison.

As for the other solutions, their lower plasma density leads to a considerably higher relative contribution of the radiative component. Very close to the Sun (1.5 $R_\odot$) the outflow velocities are so low to be very close to the static corona limit and the line ratio are almost the same for all the solutions; the slight differences are due to the small contribution of the collisional component which increases with density.

Solutions 4 and 8 show a significant decrease because the increasing velocity vs. r/$R_\odot$ leads to an increasing Doppler dimming which depletes more and more the radiative contribution: the collisional contribution thus becomes more important and the intensity ratio decreases. These two solutions reach outflow velocities higher than 200 km s^{-1} already at about 2.5 $R_\odot$.

As far as the observations are concerned, the only ones available are those by Peres et al. (1997). None of the model solutions fit reasonably well the experimental data. The discrepancies are moderate for *low-and-intermediate* density solutions (set A and B) and very large for the *high density* solutions (set C).

Fig. 6 shows the O VI line ratios vs. heliocentric distance. It is worth noting that the purely collisional value of this ratio is 0.5 and the purely radiative value is 0.25 (typical of a static corona).

Solutions with low density and outflow velocity values (1 and 2 of set A) have a ratio very close to 0.25 with a slight increase with heliocentric distance due to the start of the pumping by the C II 1037.018 Å. Those of equally low density but higher velocity (3 and 4 of set A) have line ratios slightly higher at 1.5 $R_\odot$ and increasing more rapidly vs. r/$R_\odot$. They reach local maxima where the pumping effect of the two chromospheric C II 1037.018 Å and C II 1036.34 Å lines is maximum (i.e. at 170 km s^{-1} and 360 km s^{-1}, respectively).

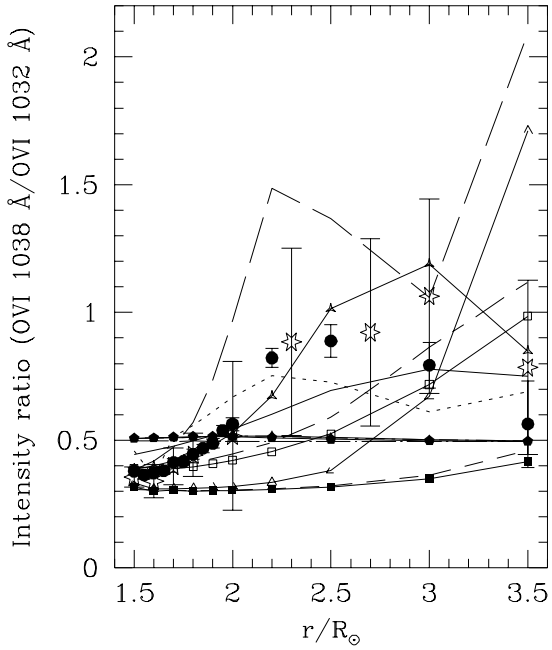

Fig. 6. O VI intensity ratio vs. heliocentric distance for all the considered wind solutions. The data points by Peres et al. (1997) (full dots) and Cranmer et al. (1999) (stars) are also reported for comparison.

More generally we note that the pumping effect on the ratio is more evident for higher relative contribution of the radiative component.

Model solutions of set B show a similar behaviour, while those of set C have an intensity ratio very close to the collisional value, as expected for *high density* solutions.

The comparison between the intensity ratio curves and the observations points out that solution 13 (generated with the constraint of reproducing the O VI line ratios found by Peres et al. (1997) and by Cranmer et al. (1999)) fits both sets of data points in the 1.5–2 $R_\odot$ range of heliocentric distances, fitting better, within the observational uncertainties, Cranmer et al. (1999) observations in all the range of heliocentric distances here examined.

5. Conclusions

In this work we have adopted specific model solutions of fast solar wind and synthesized from them the emission in the H I Lyα, H I Lyβ, and O VI resonance doublet lines, in order to identify possible diagnostics of the solar wind to be used as a guideline for the SOHO/UVCS data analysis and interpretation. The relevant spectroscopic data can help us to discriminate among fast wind solutions with different radial profiles of plasma density, temperature and outflow velocity, and to relate these differences to the momentum deposition by Alfvén waves propagating in the wind. We have found that such a diagnostics is particularly effective if the plasma density at the base of the transition region is not higher than 10^{10} cm^{-3} and that several features (intensity distributions, intensity ratios, etc.) of the line emission can be used as independent diagnostic tools; the joint use of many of them can be even more effective.

The analysis of the radial profile of the line intensities can give us a first cut diagnostics since it depends on the plasma density and velocity and their dependence gets stronger for increasing heliocentric distances.

The intensity ratios of the H I Lyα and Lyβ lines, as well as of the O VI lines, appear to be even more effective diagnostic tools of the coronal plasma conditions. The Lyα/Lyβ ratio, indeed, strongly depends on the density at the base of the transition region: solutions with $n_{p_\odot}$ lower than – or equal to – 10^{10} cm^{-3} yield values of the intensity ratio which change only slightly from one solution to another, but are significantly different from those of the highest density solutions. The O VI intensity ratio, on the other hand, is very sensitive to the outflow velocity and, on this basis, we can identify the solar wind condition (or conditions) for which the additional momentum deposition by Alfvén waves occurs close to the solar surface (e.g., solution 4 of set A). Moreover, the O VI doublet line ratio allows us to identify the high density solutions, characterized by a value close to that obtained for purely collisional conditions (0.5) all over the range of heliocentric distance which we considered.

Finally, we have looked for a possible match with observations comparing our results with the most recent data on polar coronal holes obtained by SOHO/UVCS (Peres et al. 1997; Cranmer et al. 1999).

While the drops observed in the Lyα and Lyβ intensities are well reproduced by the line simulations for solution 4 (the most affected one by Alfvén waves momentum deposition) and, to a minor extent, for solutions 8 and 13, the steeper drop of the observed O VI intensities with the heliocentric distance, which does not fully agree with our solutions, could be due either to a steeper density decrease or to a steeper outflow velocity increase (or both). In this case, however, also the Lyα and Lyβ intensities should drop more steeply than observed.

Note that the density profiles of the solutions in set A and solution 13, reproduce quite well the radial dependence of the mean electron density in coronal holes reported by Kohl et al. (1998) and Cranmer et al. (1999) (see Fig. 7a). The outflow velocity of oxygen ions ($\simeq 400$ km s^{-1} at 2.5–3 $R_\odot$), in the empirical model of coronal holes developed by Cranmer et al. (1999), is instead considerably higher (1.5–2 times) than that of protons and neutral hydrogen (see Fig. 7b). This difference could explain the discrepancy we find in the O VI intensity profile, while leaves the results obtained for the Lyα and Lyβ intensities unchanged: in our calculations we have assumed equal outflow velocity for protons and O VI ions.

The observed Lyα/Lyβ intensity values (Peres et al. 1997) at 1.5 and 3.0 $R_\odot$ are different from what obtained from the solutions of set C and, to a minor extent, also from those of solutions of sets A and B. In the light of the specific diagnostics capability of the Lyα/Lyβ intensity ratio, discussed before, we can infer that this discrepancy could be due to a density value at the base of the transition region slightly higher than 10^{10} cm^{-3}, but not as high as 5×10^{10} cm^{-3}. Anyway, at present the lack

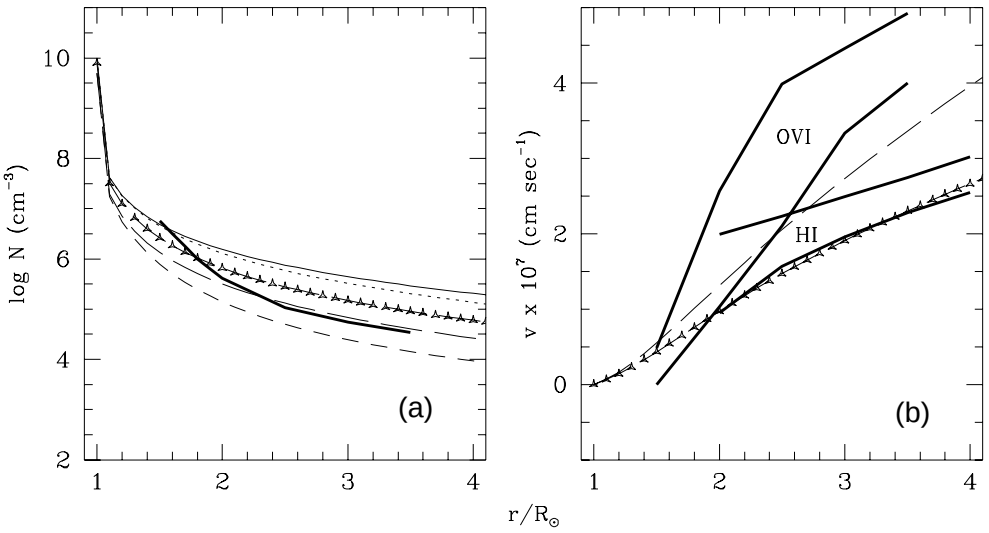

Fig. 7. a Radial profiles of density for solutions of set A and solution 13 (symbols are the same as in Fig. 1), and empirical density curve as deduced by Kohl et al. (1998) and Cranmer et al. (1999) (heavy line). **b** Radial profiles of outflow velocity for solutions 4 and 13 (symbols are the same as in Fig. 1). The empirical constraints on H I and O VI outflow velocities, deduced by Kohl et al. (1998) and Cranmer et al. (1999), are also reported as regions bordered by thick solid lines.

of a large data base of published Lyβ intensity observations prevent us from reaching any firmer conclusion.

As far as the O VI intensity ratios are concerned, the best agreement between simulations and observations (Peres et al. 1997; Cranmer et al. 1999) is found for solution 13 whose parameters, on the other hand, have been selected to fit the O VI line ratios observed. However the radial profile of the outflow velocity of solution 13 is consistent with that derived by Cranmer et al. (1999) for neutral hydrogen (see Fig. 7b), while that derived for O VI ions (see Fig. 7b) is better fitted by the velocity radial profile of solution 4. At the same time the O VI intensity ratio for solution 4 is significantly different from observations (Fig. 6).

This discrepancy could be solved by taking into account the non-thermal broadening of the coronal absorption profile of the oxygen ions (along the direction of the incident chromospheric radiation) (Kohl et al. 1997), as discussed by Cranmer et al. (1999). If this is the case, the O VI intensity ratio of solution 4 could become more similar to the observations: the effect of such a broader coronal absorption profile would be the merging of the two distinct rises obtained for solution 4 (see Fig. 6) into a single, broader and lower maximum occurring for speeds between 170 and 360 km s^{-1} (see Dodero et al. 1998).

Besides giving us a useful diagnostics of the wind conditions, this study points out some critical aspects which could lead to future model developments: to account for an additional mechanism to accelerate heavy ions preferentially and to consider that coronal absorption profiles are broader than the purely thermal ones.

Acknowledgements. We wish to thank Steve Cranmer for providing us with the values of intensities, intensity ratios and relevant uncertainties plotted in Fig. 6 of his paper. Giovanni Peres and Salvatore Orlando have also provided the values of intensities, intensity ratios and relevant uncertainties plotted in Figs. 4 and 5 of their paper. We would like to thank also the referee Prof. C. de Jager for helpful comments and suggestions which led to improve the paper. This work has been supported in part by the Italian Ministero dell'Università e della Ricerca Scientifica e Tecnologica and the Agenzia Spaziale Italiana.

References

An C.-H., Musielak Z.E., Moore R.L., Suess S.T., 1989, ApJ 345, 597
Axford W.I., McKenzie J.F., 1992, Solar Wind Seven. Pergamon Press, 1
Beckers J.M., Chipman E., 1974, Sol. Phys. 34, 151
Cranmer S.R., Kohl J.L., Noci G., et al., 1999, ApJ 511, 481
Dodero M.A., Antonucci E., Giordano S., Martin R., 1998, Sol. Phys. 183, 77
Domingo V., Fleck B., Poland A.I., 1995, Sol. Phys. 162, 1
Esser R., Habbal S.R., Coles W.A., Hollweg J.V., 1997, JGR 102, 7063
Geiss J., Gloeckler G., von Steiger R., et al., 1995, Sci 268, 1033
Gouttebroze P., Lemaire P, Vial J.C., Artzner G., 1978, ApJ 225, 655
Hollweg J.V., 1990, JGR 95, 14893
Kohl J.L., Withbroe G.L., 1982, ApJ 256, 263
Kohl J.L., Esser R., Gardner L.D., et al., 1995, Sol. Phys. 162, 313
Kohl J.L., Noci G., Antonucci E., et al., 1997, Sol. Phys. 175, 613
Kohl J.L., Noci G., Antonucci E., et al., 1998, ApJ 502, L127
MacGregor K.B., Charbonneau P., 1994, ApJ 430, 387
Maltby P., 1968, Sol. Phys. 5, 3
McKenzie J.F., Banaszkiewicz M., Axford W.I., 1995, A&A 303, L45
Moore R.L., Musielak Z.E., Suess S.T., An C.-H., 1991, ApJ 378, 347
Musielak Z.E., Fontenla J.M., Moore R.L., 1992, Phys. Fluids B 4, 13
Noci G., Kohl J.L., Withbroe G.L., 1987, ApJ 315, 706
Noci G., Kohl J.L., Antonucci E., et al., 1997 Proceedings of the Fifth SOHO Workshop, ESA-SP 404, p. 75
Olsen E.L., Leer E., Holzer T.E., 1994, ApJ 420, 913
Orlando S., Lou Y.-Q., Rosner R., Peres G., 1996, JGR 101, 443
Peres G., Ciaravella A., Betta R., et al., 1997, Proceedings of the Fifth SOHO Workshop, ESA-SP 404, p. 587
Phillips J.L., Bame S.J., Feldman W.C., et al., 1995, Sci 268, 1030
Romoli M., Fineschi S., 1994, Space Sci. Rev. 70, 359
Sandbæk Ø., Leer E., 1994, ApJ 423, 500
Spadaro D., 1998, Mem. Soc. Astron. Ital. 69, 677
Spadaro D., Ventura R., 1993, A&A 276, 571
Spadaro D., Ventura R., 1994a, A&A 281, 245
Spadaro D., Ventura R., 1994b, A&A 289, 279
Spadaro D., Ventura R., 1996, A&AS 115, 531
Velli M., 1993, A&A 270, 304
Ventura R., Spadaro D., 1999, A&A 341, 264
Withbroe G.L., 1988, ApJ 325, 442
Withbroe G.L., Kohl J.L., Weiser H., Munro R.H., 1982, Space Sci. Rev. 33, 17